The Amazon River plume—a Lagrangian view

Joachim W. Dippner [ORCID],[1]* Joseph P. Montoya,[2] Ajit Subramaniam [ORCID],[3] Jacqueline Umbricht,[1] Maren Voss[1]
[1]Leibniz Institute for Baltic Sea Research Warnemünde, Rostock, Germany
[2]School of Biological Sciences, Georgia Institute of Technology, Atlanta, Georgia, USA
[3]Lamont Doherty Earth Observatory at Columbia University, New York, USA

Abstract

Hydrographic data, nutrient data and bulk rates of nitrate uptake and primary production were determined in the Amazon River plume (ARP) in the Western Tropical North Atlantic (WTNA) during three cruises in May 2018, June/July 2019, with RV Endeavor and April/May 2021 with RV Meteor. Using daily quasi-geostrophic surface velocity data from satellite observations, the geographical positions of the stations of observations were transformed onto Lagrangian coordinates to obtain a dynamically coherent and consistent spatial distribution. After the transformation, the observed surface salinity and temperature fields were consistent with the flow fields, the ARP formed a coherent structure and the retroflection of the North Brazil Current became visible. By transforming other surface variables such as nitrate concentration, photosynthetically available radiation, turbidity, bulk rates of nitrate uptake, and primary production onto Lagrangian coordinates, patterns became consistent with the physical variables at the surface. The use of "synchronous" fields as done here by transformation onto Lagrangian coordinates is essential for spatially structured analyses of data collected over tens of days in a highly dynamic region characterized by complex flow fields with low persistence such as the WTNA. Therefore, the use of the Lagrangian method provides a powerful tool for exploring spatial distributions of biologically relevant factors in regions with complex and dynamic flow patterns. These spatial distributions are qualitatively in agreement with satellite images of daily sea surface temperature and composites of monthly mean Chlorophyll a distributions.

Challenges of ship-based observations

In general, hydrographical measurements are conducted by one or several ships occupying a series of oceanographic stations along specific tracks. In this context, two different problems arise, which have been discussed by Defant (1950). The first problem is to obtain the best possible synoptic picture of various oceanographic variables. This is a serious problem especially when the duration of a hydrographic survey extends over weeks or even months and the circulation fields are complex and characterized by high spatial and temporal variability and low persistence. The second problem can even make the observations worthless or meaningless: periodic variations of temperature and salinity owing to tidal aliasing, which results in a biased picture of the distribution of hydrographic variables owing to insufficient sampling intervals (Defant 1950). It is possible to eliminate the tidal aliasing from in situ observations by a projection onto Lagrangian coordinates, which transforms the observations from a grid fixed in space to a synoptic and synchronous grid. This has been demonstrated, e.g., on the spatial distribution of hydrographic data in the southern North Sea (Brockmann and Dippner 1987) and on nitrogen fixing cyanobacteria in the vicinity of the entrance of the Mekong River into the South China Sea (Bombar et al. 2011).

Both problems are of major relevance in the Amazon River plume (ARP) in the Western Tropical North Atlantic (WTNA) where it is rather difficult to obtain a synoptic picture of hydrographic variables (Curtin and Legeckis 1986; Geyer and Beardsley 1995) because the system is physically complex and forced by huge fresh water inputs, strong tidal currents, variable currents driven by the trade winds, and a western boundary current, all of which are located in the area of the intertropical convergence zone (ITCZ). The physics of this area and its variability is widely described (e.g., Curtin 1986*a*, 1986*b*; Lentz 1995*a*, 1995*b*; Lentz and Limeburner 1995; Geyer et al. 1996). The study area is connected to the WTNA

*Correspondence: dippner@io-warnemuende.de

circulation patterns and their strong seasonal variability in response to the dynamics of the ITCZ (e.g., Molinari 1983; Flagg et al. 1986; Johns et al. 1990). All these processes vary in time, with differences in both amplitude and duration, which is briefly outlined below.

The Amazon River

The Amazon River is the world's largest river in terms of freshwater discharge with an outflow of 80,000–250,000 m^3 s^{-1} (Oltman 1968; Dai and Trenberth 2002). The seasonal variability of the ARP and its front on the narrow shelf and in the WTNA is documented in numerous studies and has been extensively visualized in satellite images (NASA 1989) and in model results (Coles et al. 2013). The Amazon River transports roughly one cubic kilometer of sediment per year to the shelf (Meade et al. 1985) and the river discharge is so strong that no salt–water wedge enters the Amazon estuary at any stage, low or high of river discharge (Gibbs 1970). The plume is generally 5–10 m thick with a salinity of 20–30 (Geyer et al. 1996) and a plume width that varies between ∼ 80 km over the shelf and ∼ 250 km offshore (Lentz and Limeburner 1995). Vertical stratification develops from about 60–185 km offshore during low river discharge and from about 80–230 km offshore during high river discharge (Gibbs 1970). Depending on the wind forcing, the ARP was classified into intermediate, slow, and fast structures on the Brazil Shelf by Geyer et al. (1996), whereas Coles et al. (2013) identified four seasonally different pathways of the ARP in the WTNA.

The near-coastal area

In the near-coastal area tides are the dominant forcing with a pronounced spring–neap cycle with maximum velocities up to 2 m s^{-1} during spring tides and 0.7 m s^{-1} during neap tides (Geyer et al. 1991). The M$_2$-tidal current ellipses are oriented normal to the coastline (Beardsley et al. 1995), which accelerates or retards the inflow of the ARP on the Brazil shelf depending on the tidal phase and also modulates the position of the ARP over the inner shelf on a semidiurnal time scale. Observations at anchor stations indicated relatively weak changes at the seabed in response to the tides on a diurnal time scale, but much more distinct changes on a fortnightly spring–neap cycle (Nittrouer et al. 1991).

The tropical Atlantic

The circulation in the Tropical South Atlantic is driven by the South Equatorial Current (SEC), which forms three bands, the Northern, Central, and Southern SEC separated by the South Equatorial Undercurrent and the South Equatorial Countercurrent (Molinari 1983). Off Brazil, the central SEC forms the surface-intensified North Brazil Current (NBC) west of 35°W and then crosses the equator northward (Tomczak and Godfrey 1994; Stramma and Schott 1999). The NBC, which is characterized by a maximum velocity core with a

seasonally varying vertical extent (Bourles et al. 1999; Neto and Silva 2014), continues into the Guyana current (GC) and propagates into the Caribbean Sea during September–November (Richardson and Reverdin 1987). Between 5°N and 10°N, the NBC retroflects eastward seasonally and transports Amazon water into the North Equatorial Countercurrent (NECC). This retroflection of the NBC occurs from May to September with a weak current magnitude in April/May a strong current in June/July, when ITCZ change the direction, and a reduced flow in August/September (Richardson and Reverdin 1987; Müller-Karger et al. 1988; Coles et al. 2013). The region of the NBC retroflection is an eddy-rich environment, which is characterized by the formation of five to six anticyclonic warm rings per year (Gouveia et al. 2019). The low-frequency current fluctuation in this area is driven by a 40- to 60-day oscillation (Johns et al. 1990). On interannual time scales, an empirical orthogonal function analysis indicated a strong sea surface salinity (SSS) pattern along the coast that was connected to negative rainfall anomalies covering the Amazon basin that are linked to El Niño events (Tyaquiçã et al. 2017).

Seasonality

The seasonal variability of the ARP pathways owing to the changing position of the ITCZ has been described by Coles et al. (2013). When the ITCZ is at its southernmost position during December, onshore winds force the ARP against the continental margin inhibiting entrainment of the ARP into the NBC and resulting in a slow northwestward propagation of the ARP. Although the propagation of the ARP is slow, the velocity fields are characterized by pronounced spatial heterogeneity with a mean along-shelf flow of 0.72 m s^{-1} at one mooring station and of 0.36 m s^{-1} at a neighboring station roughly 50 km further offshore (Lentz 1995a). In April and May, when the ITCZ migrates to the north and the Amazon runoff reaches its maximum, the onshore wind weakens and the ARP spreads into the NBC and GC. The result is fast transport in a northwestward direction but also eastward into the tropics. In June, the ITCZ reaches its northernmost point, driving a retroflection of the NBC, which intensifies the NECC and increases the transport of the ARP into the Central Tropical Atlantic. When the ITCZ moves southward, the retroflection of the NBC and the NECC is reduced.

Previous experiments

Various experiments have been performed to understand and visualize the complexity of the seasonality of the flow field and the variability of the M$_2$ tide using surface drifters or satellite tracked drifting buoys (Molinari 1983; Richardson and Reverdin 1987; Müller-Karger et al. 1988; Limeburner et al. 1995) and model simulations (Coles et al. 2013). Limeburner et al. (1995) launched satellite-tracked drifters near the mouth of the Amazon River. The drifters moved along the shelf with a mean

speed varying from 0.41 to 1.28 m s^{-1} and strong cross-shelf variability. When drifters were advected into deeper water, they began looping in anticyclonic eddies with a period of ~ 11 d. The drift experiment of Müller-Karger et al. (1988) showed that the discharge of the Amazon River is carried offshore by the retroflection of the NBC into the NECC and can be traced thousands of kilometers into the WTNA. The complexity of seasonal advection patterns has been documented with model simulations using Lagrangian tracers to visualize the circulation patterns in the WTNA (Coles et al. 2013) and the transport of suspended matter from the NBC into the Caribbean Sea (Allende-Arandia et al. 2023).

One of the most surprising results of the physical observations of a multidisciplinary amazon shelf sediment study (AMASSEDS) was the strong variability in the currents and salinity of the ARP on time scales of days to weeks (Geyer et al. 1991; Lentz 1995b). These variations are driven by wind fluctuations over 7–10 d periods (Curtin and Legeckis 1986) and result in salinity variation of over 10 on time scales of days to weeks (Curtin 1986b; Lentz and Limeburner 1995). The driving forces on the Amazon shelf produce distinct temporal and spatial variability, which control the fate of the material that is discharged from the river mouth. The ARP carries large amounts of sediments, nutrients as well as chromophoric dissolved organic material (CDOM), which makes the ARP visible from space as a greenish-brown plume stretching more than a thousand of kilometers into the WTNA (Del Vecchio and Subramaniam 2004).

Classification and biological aspects

The importance of salinity in determining the distribution of different phytoplankton communities has been highlighted by Goes et al. (2014) in the Amazon influence on the Atlantic: Carbon export from nitrogen fixation by diatom symbioses (ANACONDAS) project. Based on the work of Subramaniam et al. (2008), they separated their stations into three groups, an oceanic type with high salinity $S > 35$, an estuarine type with $S < 28$, and a mesohaline type with $30 < S < 35$. This classification was the starting point for a comprehensive delineation of phytoplankton habitats in the ARP and the WTNA (Weber et al. 2019; Pham et al. 2024). Different biological aspects of the ARP system have been investigated, such as the nitrogen cycle and nitrogen uptake rates (Umbricht et al. 2024), nitrogen cycle in the sediment (Choisnard et al. 2023), nitrogen fixation and export production in the WTNA (Weber et al. 2017; Montoya et al. 2019), and growth efficiency of zooplankton in the ARP (Loick-Wilde et al. 2016). In the context of climate change, a significant CO_2 sink in the WTNA has been identified in the ARP (Körtzinger 2003) as well as an enhanced carbon sequestration (Subramaniam et al. 2008).

Dynamically consistent patterns

The high variability of the ARP system in both time and space strongly influences the interpretation of hydrographic surveys. This variability is the main reason why it is rather difficult to obtain a synoptic picture of the system (Curtin and Legeckis 1986; Curtin 1986b; Geyer and Beardsley 1995). If the circulation fields are characterized by a high complexity as mentioned above combined with high spatial and temporal variability and low persistence, a quasi-synoptic plot of hydrographic variables in an Eulerian grid may result in meaningless distributions. Here, we show that a transformation onto Lagrangian coordinates results in dynamically consistent patterns of different physical and environmental variables. This method is applied to three different cruises in the ARP and compared with satellite images of chlorophyll (Chl *a*) (Sathyendranath et al. 2019) and sea surface temperature (SST) observations (Good et al. 2020).

Materials and procedures

Field data

Water samples were taken in the WTNA during the period from April to July aboard the R/V Endeavor and R/V Meteor during three cruises (EN614 from May 6 to June 1, 2018, EN640 from June 13 to July 10, 2019 and M174 from April 21 to May 30, 2021). Cruises EN614 (20 stations) and EN640 (20 stations) focused on the northern and north-western parts of the ARP, while the southern plume and the river estuary were sampled more extensively during M174 (18 stations). A Seabird SBE-911 CTD-rosette system was used to measure hydrographic variables and collect water samples for the analysis of nitrate, nitrite, phosphate, silicate, and phytoplankton. The temperature sensor covers a range of $-2°C$ to $35°C$ with an accuracy of 1 mK, and the conductivity sensor the range 0–7 S/m with an accuracy of 0.0003 S/m. The CTD was equipped with a turbidity sensor WET Labs FLNTURTD measuring turbidity in nephelometric turbidity units (NTU). Sampling depths included surface water, the mixed layer and the depth of the chlorophyll maximum determined from CTD fluorescence profiles. The maximum sampling depth was chosen based on the intensity of photosynthetically available radiation (PAR) measured with a biospherical QSP200L4S sensor mounted on the rosette: 0.1% of surface irradiance on cruises EN614 and EN640 and 1% surface irradiance on cruise M174. We also used the 1% light level to define the lower limit of the euphotic zone. Further details on sampling procedure were given in Umbricht et al. (2024).

Satellite data

Daily gridded velocities were obtained from the EU Copernicus Marine Service Global Ocean Gridded L4 Sea Surface Heights Product (QUID 2018). This product is produced by the SL-TAC multi-mission altimeter data processing system using data from all altimeter missions: Jason-3, Sentinel-3A, HY-2A, Saral/AltiKa, Cryosat-2, Jason-2, Jason-1, T/P,

ENVISAT, GFO, and ERS1/2. The geostrophic current products were computed using a 9-point stencil width method (Arbic et al. 2012) for latitudes more than 5°N/S of the equator. In the equatorial band, the Lagerloef method introducing the *β*-plane approximation was used (Lagerloef et al. 1999). Details on the procedure, including how the products were processed, are given in Pujol et al. (2016). These daily velocity fields, which have a spatial resolution of 0.25°, were extracted for the period of the three cruises. The daily mean velocity fields averaged over the duration of the cruises are shown in Fig. 1, to visualize the complexity and high variability of the circulation patterns in the WTNA during different months. In addition, satellite-derived composites of monthly Chl *a* distributions observed in May 2018, June 2018, and May 2021 were used for comparison as well as selected daily SST observations. Monthly composites of Chl *a* for May 2018, June 2019, and May 2021 were derived from the ocean color climate change initiative product with a 4 km resolution. These composites were based on a merger of SeaWiFS, VIIRS, MERIS, MODIS-Aqua, OLCI-S3A, and OLCI-S3B data using the best-performing atmospheric correction and chlorophyll algorithms, with a temporally weighted bias correction aiming to minimize differences among sensors (Sathyendranath et al. 2019).

We used the operational SST and ice analysis (OSTIA) produced by the UK Met Office. The OSTIA global foundation SST product provides daily, gap-free maps of SST at 0.05° × 0.05° horizontal grid resolution, using in-situ and satellite data from both infrared and microwave radiometers (Good et al. 2020).

Lagrangian coordinates

For questions of mass transport in the ocean or the atmosphere, the motion of the fluid elements is of prime interest so a coordinate system that is transported by the fluid, i.e., a Lagrangian system, is often much more appropriate than one fixed to the surface of the Earth, i.e., a Eulerian system. While the Eulerian view describes the basic characteristics of a velocity field, the Lagrangian view is focused on transport phenomena. Consider $\vec{a}_i$ is the geographical position of any arbitrary station *i* of a ship-based observation and τ_i the actual time of measurement. Then, the fluid element where the measurements have been carried out, can be identified by its position $\vec{x}_i$, which depends upon the initial coordinate $\vec{a}_i$ and the elapsed time $\tau_e - \tau_i$. Thus,

$$\vec{x}_i = \vec{x}_i\left(\vec{a}_i, \tau_e - \tau_i\right); \quad \vec{x}_i\left(\vec{a}_i, 0\right) = \vec{a}_i \tag{1}$$

The Lagrangian velocity is defined as:

$$\frac{d}{dt}\vec{x}_i\left(\vec{a}_i, \tau_e - \tau_i\right) = \vec{u}_L\left(\vec{a}_i, \tau_e - \tau_i\right) \tag{2}$$
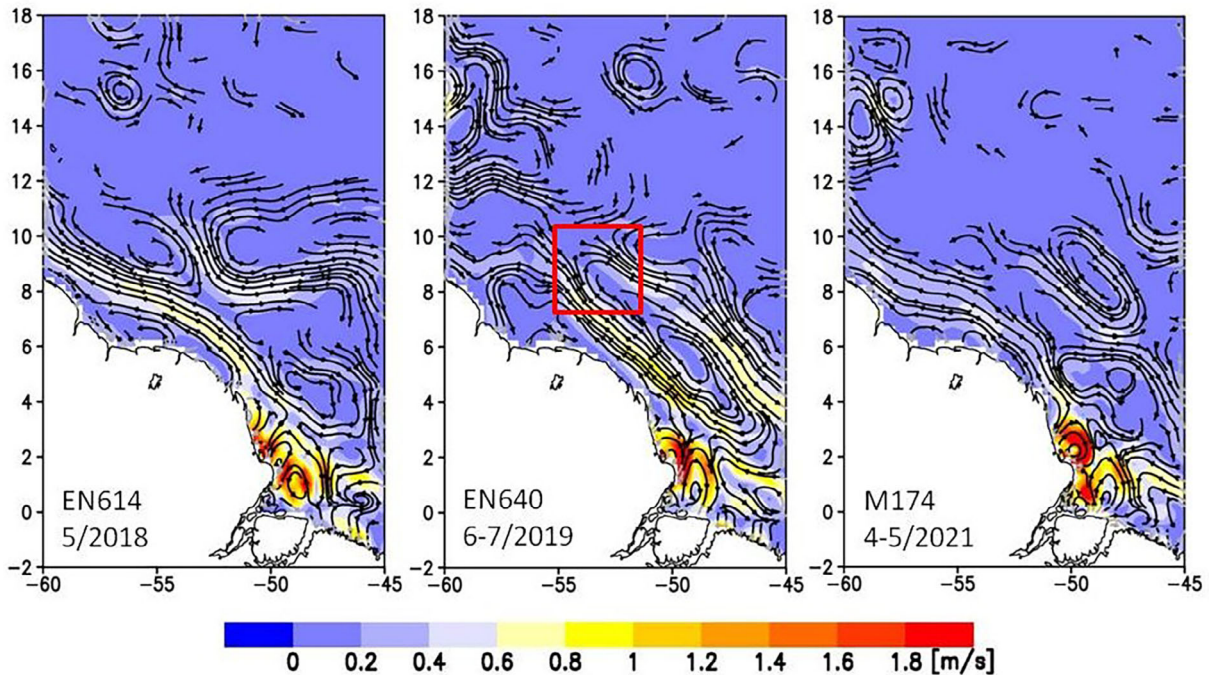

Fig. 1. Mean surface velocity during the RV Endeavor cruises EN614 in May 2018 (left), EN640 in June/July 2019 (middle), and RV Meteor cruise M174 in April/May 2021 (right). The streamlines are based on daily mean velocities derived from satellite data, which are averaged in time over the duration of the cruise. The red square marks the area of NBC retroflection.

so that:

$$\vec{x}_i - \vec{a}_i = \int_{\tau_i}^{\tau_e} \vec{u}_L\left(\vec{a}_i, \tau_e - \tau_i\right) dt \tag{3}$$

The connection between the Lagrangian velocity u_L and the Eulerian velocity U_E is given by:

$$\vec{u}_L\left(\vec{a}_i, \tau_e - \tau_i\right) = \vec{U}_E\left(\vec{x}_i\left(\vec{a}_i, \tau_e - \tau_i\right), \tau_e - \tau_i\right) \tag{4}$$

and hence:

$$\vec{x}_i - \vec{a}_i = \int_{\tau_i}^{\tau_e} \vec{U}_E\left(\vec{x}_i\left(\vec{a}_i, \tau_e - \tau_i\right), \tau_e - \tau_i\right) dt \tag{5}$$

The daily satellite velocity fields were transformed from an Arakawa A- to an Arakawa C-grid (Arakawa and Lamb 1977) and serve as the Eulerian velocity field for the computation. The transformation onto Lagrangian coordinates (integration of Eq. 5) is done with a fourth order Runge–Kutta method in time and the method of weighted distances in space. To ensure the Courant stability criterion (Roache 1976), the model runs with a time step of 10 min. The geographical position of each station is integrated from the time of measurement τ_i to the time of the last station τ_e,

which serves as a reference time for synchrony. Beside the use of satellite observed surface velocities, the difference in integration length among observations is the novel aspect in this article.

In addition, the persistence of the flow field in percent is calculated from the Eulerian velocity fields as:

$$\text{Per}\,(\%) = \left[1 - \frac{\sum \sqrt{\left(U_E - \overline{U}_E\right)^2 + \left(V_E - \overline{V}_E\right)^2}}{\sum \sqrt{\left(U_E^2 + V_E^2\right)}}\right] * 100 \tag{6}$$

U and V are the the E–W and N–S components of the flow field. Figure 2 shows the persistence of the surface flow field during the three cruises and the cruise tracks and the stations in the geographical (Eulerian) grid and in Lagrangian coordinates. SSS, SST, nitrate concentration, near-surface PAR measured at water depth of 2–5 m, turbidity and rates of primary production and nitrate uptake at the surface were also plotted in a Eulerian and a Lagrangian grid (Figs. 3–9). The reference time for synchrony for each cruise is the time of the last station τ_e, which is May 29, 2018 for EN614, July 5, 2019 for EN640, and May 13, 2021 for M174. The OSTIA SST for these days (Fig. 10) is compared with the computed Lagrangian SST distribution and the Chl *a* composites from satellite (Fig. 11) is compared with the primary production in Lagrangian coordinates.
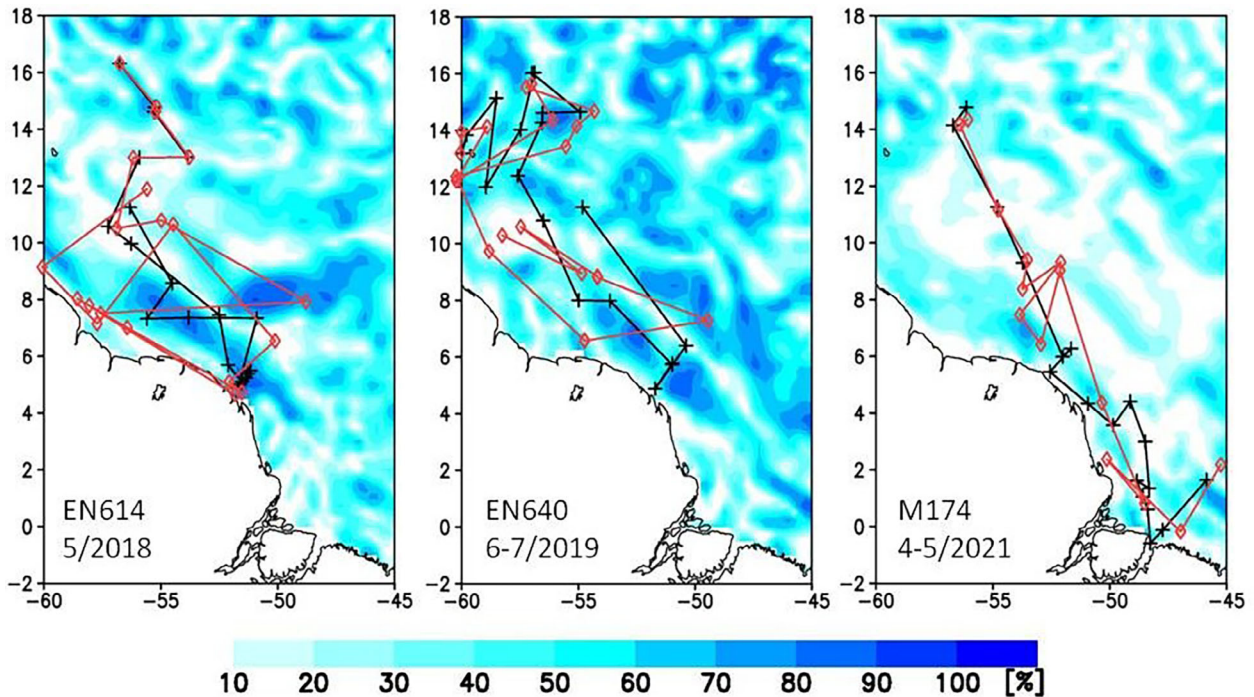

Fig. 2. Persistence of the surface flow fields during the three cruises in percent. Black line and crosses mark the cruise track and the position of sampling stations in a geographical grid (Eulerian view) and red line and diamonds in Lagrangian coordinates.
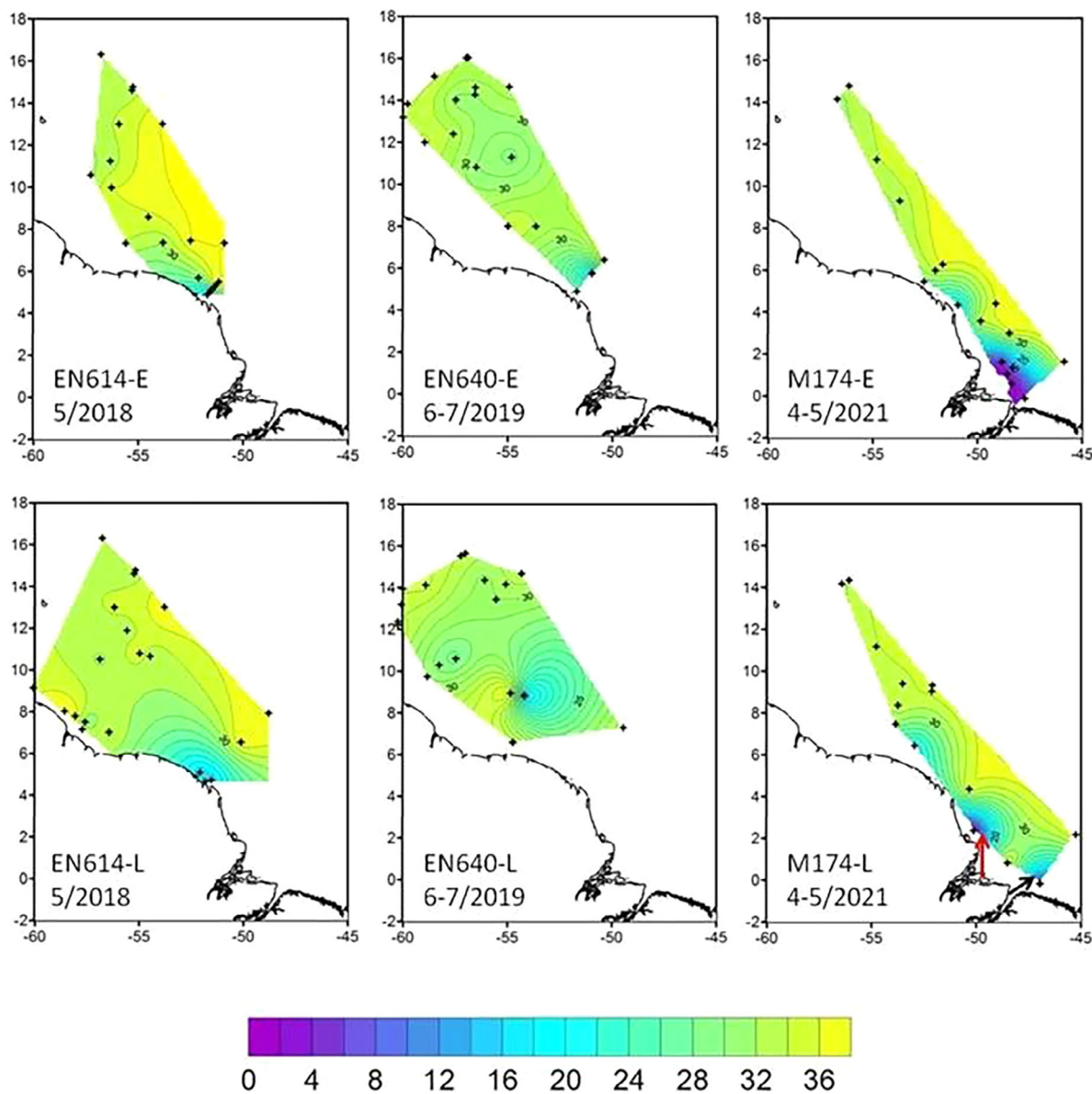
Fig. 3. SSS distribution during the cruises in a Eulerian grid (upper row) and in Lagrangian coordinates (lower row). The arrows in M174-L mark the plumes of River Amazon (red) and River Pará (black).

Results

The three cruises differed in terms of the seasonal outflow and the spatial extent of the river plume. Cruise M174 (April/May 2021) was the earliest in the year and took place before the maximum outflow, Cruise EN614 (May 2018) occurred at the beginning of the maximum outflow, while Cruise EN640 (June/July 2019) represented the situation during the maximum outflow. The intensity of the ARP outflow was consistent with the mean meridional position of ITCZ: $\sim 1°N$ in April 2021, 5°N in May 2018, and 9°N in June 2019 as identified in the NCEP/NCAR reanalysis data (Kalnay et al. 1996). The response was also visible in the variability of the velocity fields

(Fig. 1) as a change from a coast-parallel current to a typical retroflection of the ARP at $\sim 8°N$ from June onwards. The averaged quasi-geostrophic velocity fields for the three cruises (Fig. 1) showed a pronounced NBC and its continuation into the GC parallel to the coast. The NBC was strong during cruises EN614 (May 2018; duration 27 d) and EN640 (June/July 2019; 28 d), but relatively weak during cruise M174 (April/May 2021; 40 d), which might be related to the seasonality of the ITCZ or alternatively to the duration of the cruise because persistence may decrease with time.

During all cruises, strong tidal currents occurred in the mouths of the Rivers Amazon and Pará with velocities up to
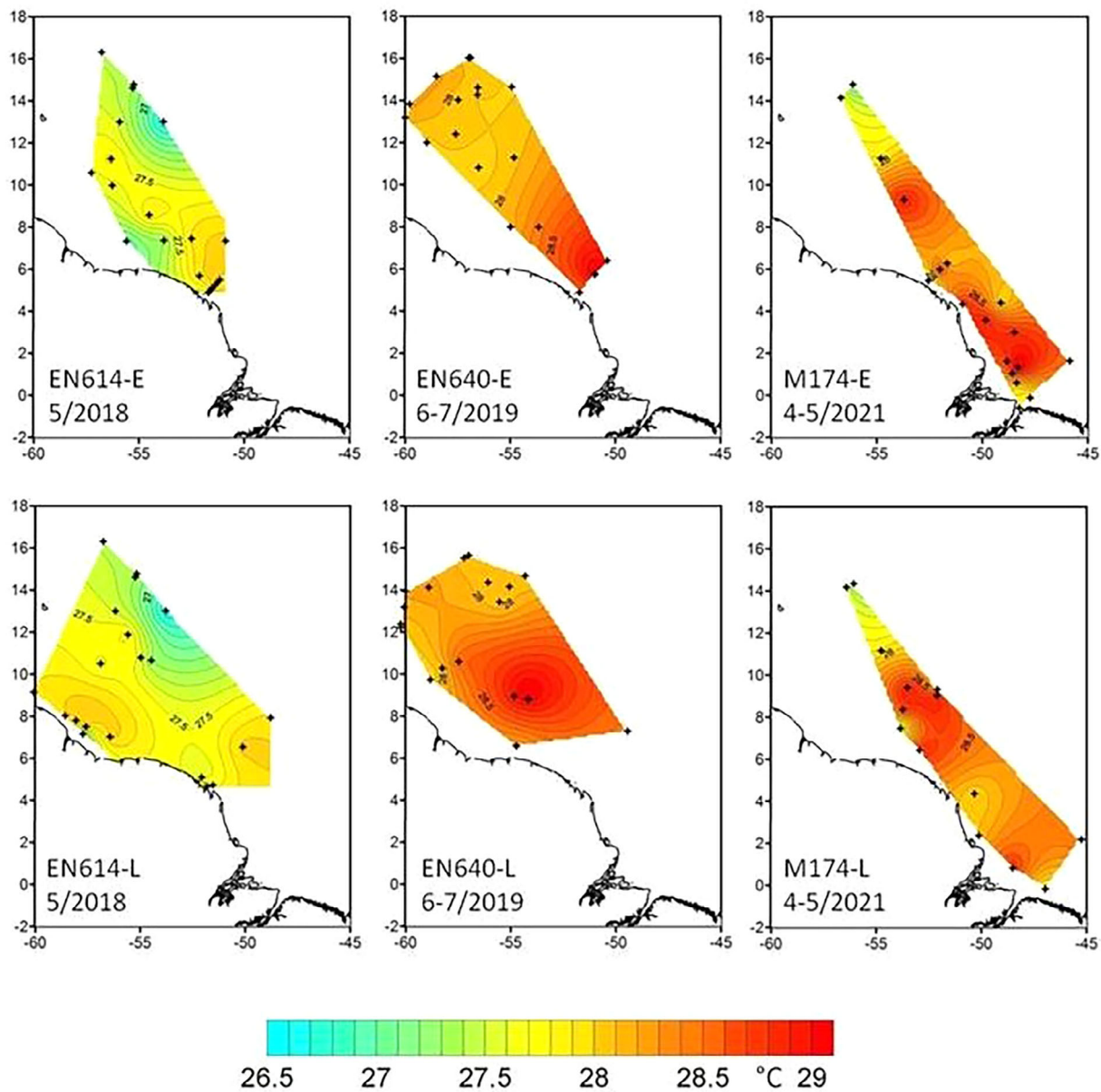
Fig. 4. SST distribution during the cruises in a Eulerian grid (upper row) and in Lagrangian coordinates (lower row).

1.6 ms^{-1}. These strong tidal currents were also observed in our vessel-mounted VM-ADCP data in the vicinity of the Amazon River mouth (Fig. 12). During June/July (EN640), a retroflection of the NBC occurred at $\sim 8°$N marked by a red square in Fig. 1. This retroflection zone was characterized by dynamic structures such as meanders or synoptic scale eddies that entrain the ARP and were detached from the NECC in the second half of the year (Bourles et al. 1999; Coles et al. 2013). In addition, the instability of the plume front caused a meandering of the ARP, which can cause local upwelling (Fratantoni et al. 1995; Fratantoni and Glickson 2002). Offshore of the NBC and the NECC the flow fields were characterized by transient eddy fields.

The variability in the flow field was visualized in the distribution of the persistence during the three cruises (Fig. 2), which showed a rather patchy distribution. Persistence was high in the region of the NBC and its retroflection, but in general low during M174 (April/May 2021), a further indication of high variability of the flow field during this cruise. These patterns of the persistence were very similar to the computed annual climatologic Lagrangian coherent structure (Fig. 2 in Allende-Arandia et al. 2023).

Our transformation onto Lagrangian coordinates led to one station being advected out of the study area during Cruise EN614 (May 2018) and a few stations during Cruise EN640 (June/July 2021). These stations were included in Fig. 2 to
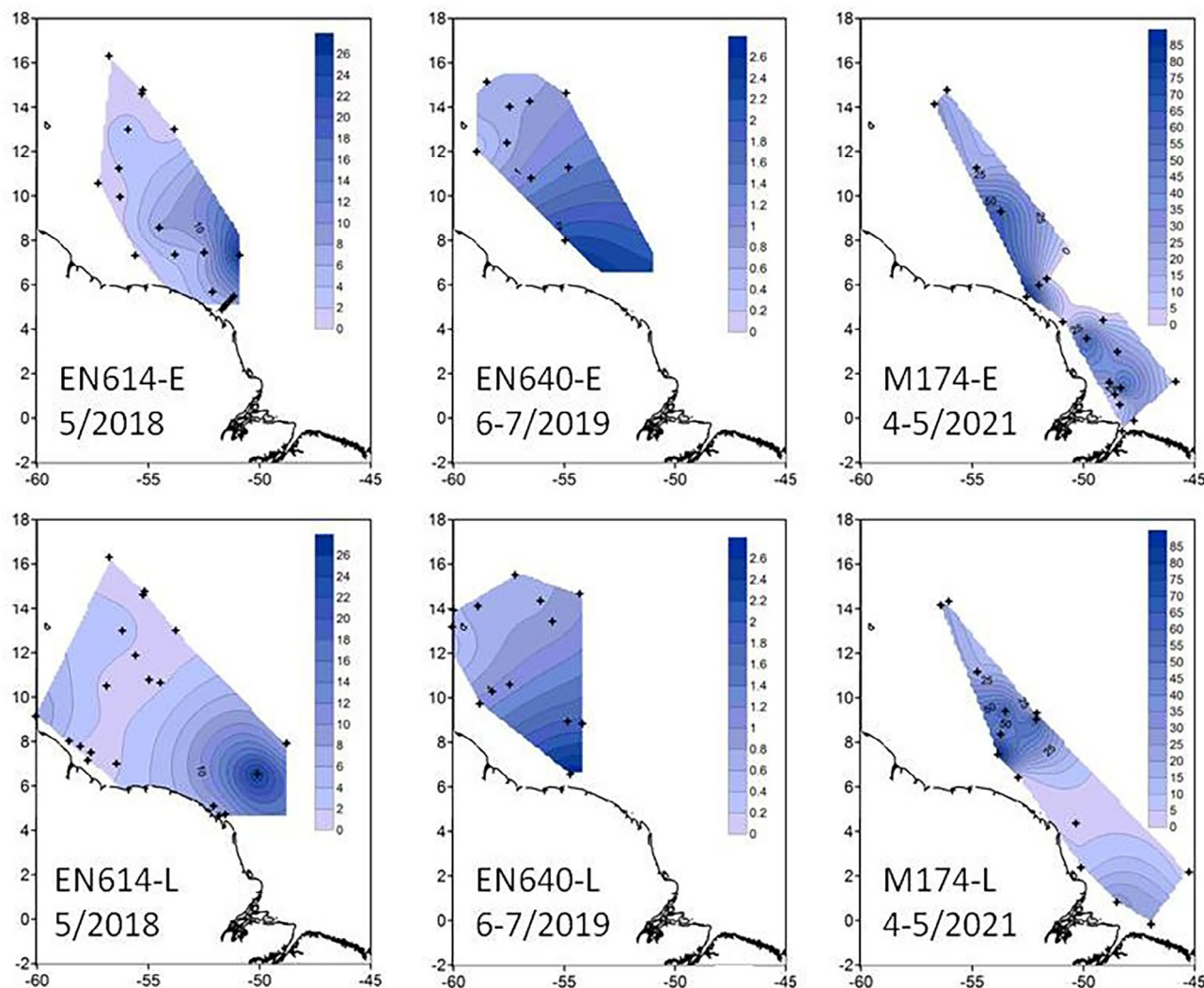
Fig. 5. Bulk nitrate uptake rate (nmol L^{-1} h^{-1}) at the surface during the cruises in a Eulerian grid (upper row) and in Lagrangian coordinates (lower row).

clarify the advection pattern, however, they were not included in our plots of variables in Lagrangian coordinates.

The SSS distribution in Eulerian coordinates (Fig. 3, upper row) shows isohalines normal to the streamlines during the cruises EN614 (May 2018) and EN640 (June/July 2019), which was not consistent with a quasi-geostrophic balance, which would require parallel streamlines and isohalines. For the same reason, the weak eddy during EN640 (June/July 2019) between 11°N and 12°N in the salinity field is not consistent with the circulation pattern. Salinities close to zero were only measured during Cruise M174, the only cruise to sample directly in the estuary. During this cruise, in April/May 2021, we found a high salinity gradient of 0.15 km^{-1} at the surface over a distance of ~200 km in Eulerian coordinates in the vicinity of the mouth of the rivers Amazon and Pará.

In the Lagrangian salinity fields (Fig. 3, lower row), isohalines were generally parallel to the streamlines (Fig. 1) indicating a consistency of salinity distribution and flow fields during both Endeavor cruises. During May 2018 (EN614) the ARP was propagating along the coast on the Brazil Shelf parallel to the shelf edge and the NBC. In addition, during June/July 2019 (EN640), an eddy with a low salinity core occurred in the retroflection zone at ~9°N, which was also consistent with the flow field (Fig. 1). This strong salinity gradient may cause baroclinic instabilities and the formation of eddies and potentially upwelling. The strong salinity gradients in the Amazon estuary during April/May 2021 (M174) disappeared in Lagrangian coordinates and both plumes of the rivers Amazon and Pará were visible. The ARP is meandering in northwest direction parallel to the coast (Curtin 1986*b*; Smith Jr. and DeMaster 1996).
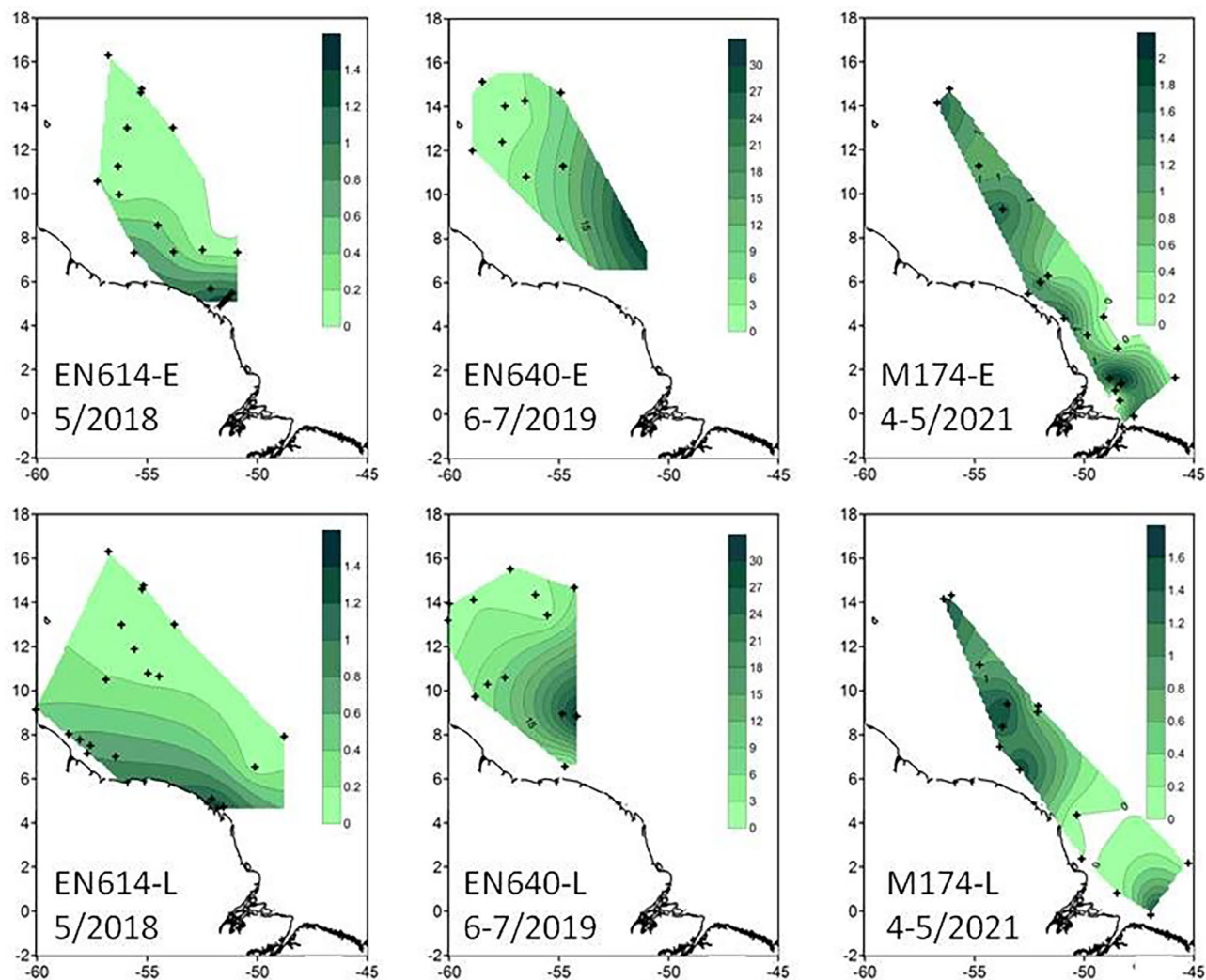
Fig. 6. Bulk primary production rate (μmol L^{-1} h^{-1}) at the surface during the cruises in a Eulerian grid (upper row) and in Lagrangian coordinates (lower row).

Similar rather unrealistic patterns occurred in the Eulerian SST fields (Fig. 4, upper row); a heterogeneous pattern during May 2018 (EN614), an east–west gradient during June/July 2019 (EN640) and a patchy distribution during April/May 2021 (M174). After the transformation onto Lagrangian coordinates the SST (Fig. 4, lower row) was consistent with the circulation patterns during our cruises (Fig. 1). For example, the jet of the NBC was flanked by a small cyclonic warm core recirculation cell between the NBC and the coast and a larger anticyclonic cold core circulation cell offshore during May 2018 (EN614). The SST field was dynamically consistent with the surface circulation field. However, the observed OSTIA SST (Fig. 10) for the reference day May 29, 2018 of the EN614 cruise showed a warm belt of the NBC flanked by two cooler water bodies. The difference was the temperature of the near coastal cell, which was warm in the computation and cold in the satellite image. This discrepancy can be explained by the

fact that the transformation onto Lagrangian coordinates was computed with horizontal velocity fields at the surface only. This quasi-geostrophic approach neglected the three-dimensionality of the flow field especially if upwelling events were of relevance in the circulation patterns.

During June/July 2019 (EN640), the SST in Lagrangian coordinates (Fig. 4, lower row) displayed a pattern similar to salinity, including a warm core eddy in the retroflection zone, which is also consistent with the flow field (Fig. 1) and the OSTIA SST for the reference day June 5, 2019 (Fig. 10). The patchy structure of the SST during April/May 2021 (M174) disappeared in Lagrangian coordinates and was instead characterized by a wavy structure extending in the northwest direction, which was also consistent with the OSTIA SST at the reference day May 13, 2021 (Fig. 10). Except the warm near-coastal recirculation cell during EN614, the computed SST in Lagrangian coordinates (Fig. 4) was qualitatively in agreement with the
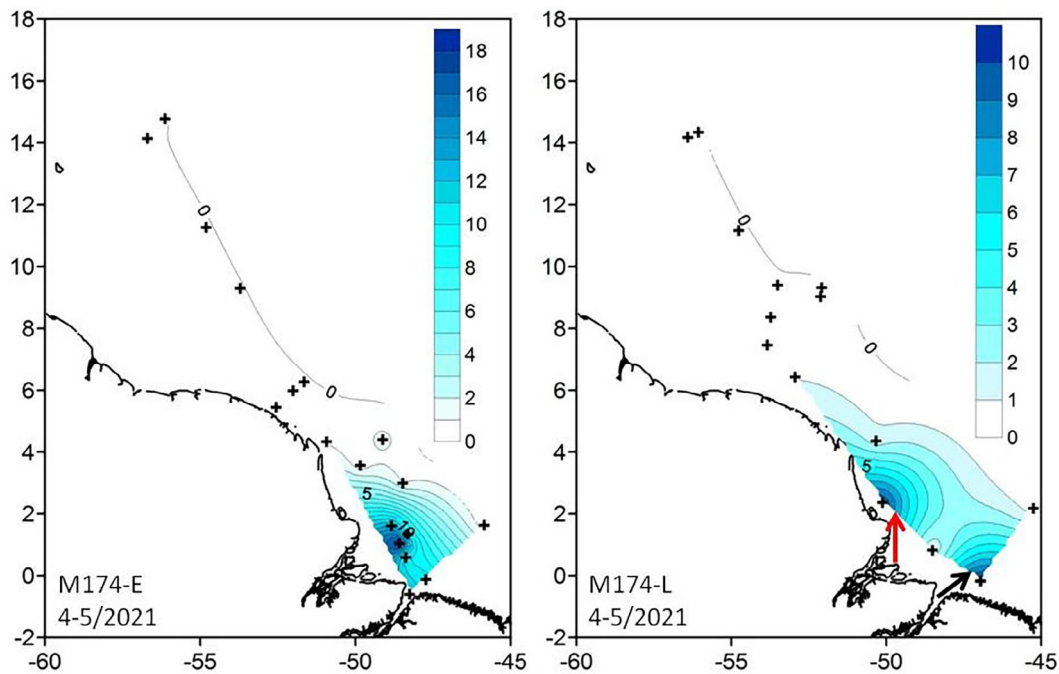
Fig. 7. Surface concentration of nitrate (μM) during the cruise M174: Left Eulerian view, right Lagrangian view. The reader may note the different scales. The arrows in M174-L mark the plumes of River Amazon (red) and River Pará (black).
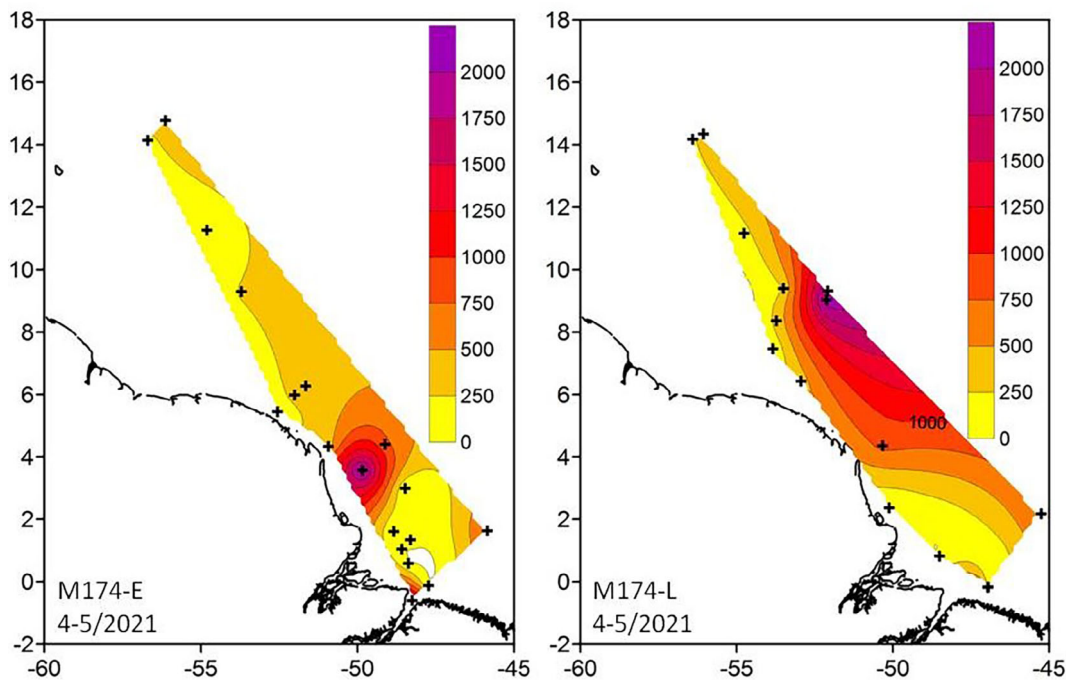
Fig. 8. Near-surface PAR (μE m^{-2} s^{-1}) during the cruise M174: Left Eulerian view, right Lagrangian view.

satellite images of the OSTIA SST for the reference days (Fig. 10).

Biological rate measurements can also be more consistently visualized in Lagrangian fields. The bulk nitrate uptake rates and the bulk primary production rates at the surface showed different absolute values and different gradients during May 2018 (EN614) and June/July 2019 (EN640). The bulk nitrate uptake rates during May (EN614) were characterized by generally high values (up to
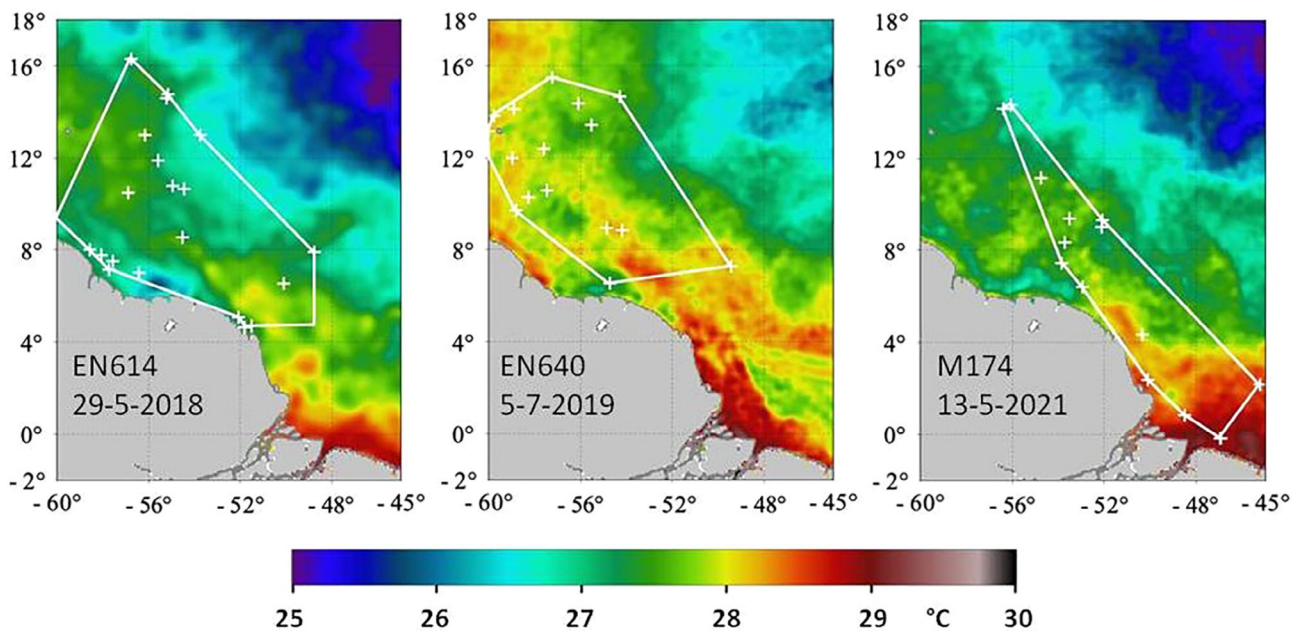
Fig. 11. Monthly composites of satellite observed Chl *a* concentration (mg/m³) for the three cruises. From left to right: May 2018, June 2019, and May 2021. White crosses mark the Lagrangian coordinates. The white line is the convex hull around all these coordinates and the covered area is identically with the area of the plotted variables.
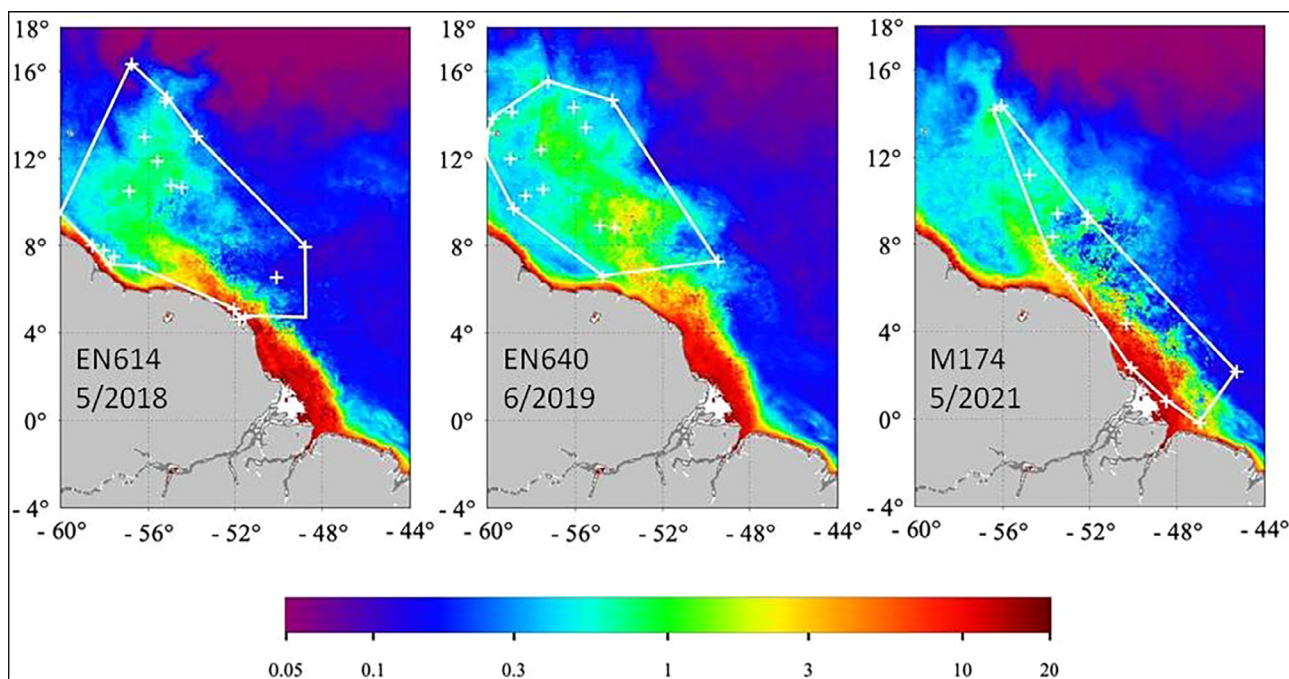
Interestingly, a transformation onto Lagrangian coordinates did not simplify the pattern when data coverage is low. The reason is that nitrate uptake and primary production rates were measured only at one third of the stations with the consequence that the fine structure from the flow field was lost and the deformation of the coordinate system was not fully reproducible with less stations. One exception was the primary production rate during June/July 2016 (EN640; Fig. 6). In this case, the distribution of rates formed a feature located
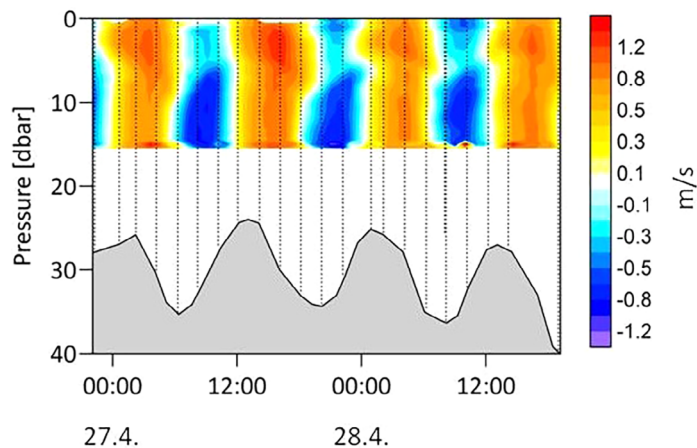

Fig. 12. Vessel mounted VM-ADCP velocities measured for 2 days in April 2021 in the mouth of River Amazon (1.35°N, −48.315°E) during cruise M174.

between 8°N and 10°N and around 55°W that was consistent with the low salinity and high temperature eddy in the retroflection zone (Figs. 3 and 4).

During April/May 2021 (M174), higher nitrate uptake rates (up to 85 nmol L^{-1} h^{-1}) were observed than during the other cruises (Fig. 5). The primary production rates (Fig. 6) were low and in a range similar to the May 2018 (EN614) values. The spatial distributions of nitrate uptake and primary production rates were not congruent. The maximum in nitrate uptake rate was located at ∼ 8°N with two smaller local maxima at ∼ 4°N and in the Amazon estuary, whereas the maximum of primary production rates occurred in front of the estuary. To get an impression of the dynamics of the primary production and the coherence to other variables, we also analyzed the distribution of surface nitrate concentration, near-surface PAR and surface turbidity (Figs. 7–9).

In the Eulerian view, similar to the SSS, nitrate concentration and turbidity exhibited an extremely strong gradient near the river mouth. The corresponding near-surface PAR showed a patchy distribution with low values between 0 and 250 *μ*E m^{-2} s^{-1}. Owing to the strong light limitation of the primary production by high turbidity at the river mouth, the maximum in primary production of 2 *μ*mol L^{-1} h^{-1} and the local maximum in nitrate uptake of 30 nmol L^{-1} h^{-1} seems biologically implausible.

In contrast, the same variables in a Lagrangian view provided a dynamically consistent picture. Similar to the SSS, the strong gradients of nitrate concentration and turbidity

disappeared and the plumes of the rivers Amazon and Pará were visible in these distributions. Near-surface PAR increased in the offshore direction, consistent with the decreasing turbidity. Salinity, nitrate concentration, turbidity, and bulk rates of nitrate uptake and primary production were characterized by a wavy structure propagating in northwest direction along the coast. In Lagrangian coordinates, the maxima in nitrate uptake and primary production rates were located in the same area between 8°N and 10°N.

Although we carried out fewer biological than physical observations, we found a qualitatively agreement between the observed primary productivity during the cruises (Fig. 6) and monthly composites of Chl *a* concentration (Fig. 11). In May 2018, a band of high primary productivity propagated parallel to the coast; in June 2019, an eddy was formed in the retroflection zone, and in May 2021 the band of primary productivity showed a patchy distribution along the coast similar to the Chl *a* composite.

Discussion

The Lagrangian tracer technique is widely used to simulate advection–diffusion–reaction processes in physical, biological or chemical environments with a central focus on nonlinear advection. Depending on the property considered, tracers can be classified as passive, active, dynamically active or interactive tracers, which is described below. Concerning pollutants, tracers can be dissolved or particle bound substances such as heavy metal or radioactive waste (Maier-Reimer 1977) or fluids like crude oil (Dippner 1983). In the case of eutrophication problems, tracers may be a concentration of nutrients like phosphate or nitrate (Dippner 1993*a*). In the context of biological questions, a tracer can also be the biomass of phytoplankton, zooplankton, harmful algae, or fish eggs and larvae (Woods and Onken 1982; Berntsen et al. 1984; Dippner et al. 2011). Finally, for specific physical questions, relevant tracers may include temperature (Bork and Maier-Reimer 1978), salinity (Maier-Reimer 1978), density of sea water (Dippner 1990, 1993*b*), as well as dynamic height (Pavia and Cushman–Roisin 1988) or potential vorticity (Maier–Reimer 1988). The technique can also be used to calculate residence times in systems such as the North Sea, the Bay of Gdansk, or the Dutch Wadden Sea (Maier–Reimer 1979; Dippner et al. 2019; Fajardo–Urbina et al. 2023). Globally, this method has been applied to the distribution of chlorophyll variability (Kuhn et al. 2023). A general overview is given in the UNESCO Encyclopedia of Life Support Systems (Dippner 2005).

In the present case, the geographical positions of the stations served as passive Lagrangian tracers, which were transported by the observed quasi-geostrophic flow fields. The novelty of our approach lies in the use of velocity data from satellite for advection and the different length of integration up to a single reference time for each cruise. Specifically, the movement of each position is integrated from the time of observation to the time of the last station, which was considered as the reference time. This means that the positions of the stations sampled near the beginning of each cruise were advected for a longer time than the stations sampled near the end of the cruise, resulting in complex advection patterns (Fig. 2) and consequent alteration in the spatial distributions of scalar variables, reflecting the horizontal deformation of the flow fields. The potential to generate synoptic and synchronous surface distributions is clearly a major strength of our approach. On the other hand, the example of the computed warm recirculation cell (EN614) revealed that a transformation using only horizontal flow fields free of divergence my produce erroneous results in areas with a pronounced vertical velocity component in the near coastal area. In other words, the primary weakness we identified relates to the flow field used and not the transformation onto Lagrangian coordinates itself. To overcome this problem and/or to consider ageostrophic velocity components, a 3-D eddy-resolving circulation model would provide better results.

Persistence of features and the time period of investigation are both essential criteria in deciding whether to use a transformation onto Lagrangian coordinates. Historically, most of our knowledge about the ocean is based on cruises, which are generally interpreted in a Eulerian coordinate system. If the time scale of the considered problem is short (advection is of minor importance) or the persistence of the flow field is high (e.g., rivers or tides) the Eulerian approach is effectively equivalent to the Lagrangian. In all other cases, e.g., transport or mixing in turbulent flows or nonlinear horizontal deformation of the flow field such as fronts, eddies or filaments (all characterized by low persistence), the use of Lagrangian method is strongly recommended.

In our study, we did not consider the impact of tides and did not eliminate the aspect of tidal aliasing, which is one of the largest source of error in satellite gravimetry (Liu and Sneeuw 2021) and would require a tidal model for the WTNA. On the other hand, a careful inspection of the tidal constituents of the M_2, S_2, N_2, and K_2 tides (Beardsley et al. 1995; Hart–Davis et al. 2021) indicated strong tidal signals on the Amazon shelf where the water depth is < 20 m. This area is a relatively small part of the Amazon shelf and the small phase variation of tidal currents and surface elevation across the shelf suggest that the semi diurnal tide is a strongly damped standing wave (Geyer et al. 1991), which might contribute to the meandering structure observed in the M174 SSS figures. Neglecting the impact of tides in this area should therefore not influence the general result of this paper. A potential improvement, particularly in this coastal region, could be the use of, e.g., the EOT20 model for the correction of tidal aliasing (Hart–Davis et al. 2021) in satellite data.

Two aspects of our data illustrate the power of transformation onto Lagrangian coordinates in constructing quasi-synoptic summaries of hydrographic observations.

Specifically, our Lagrangian approach resolved the impact of the temporal maximum in Amazon discharge, one of the most dynamic features of this system, which is linked to the often observed isolated freshwater lens (Calef and Grice 1967; Ryther et al. 1967; Gibbs 1970). Similarly, our transformation clearly separated the Amazon and Pará River plumes despite their close geographical proximity (Lentz and Limeburner 1995; Geyer et al. 1996; Smith Jr. and DeMaster 1996).

The isolated freshwater lens is an example that can be related to the impact of the ITCZ. When the ITCZ migrates to the north and the Amazon runoff reaches its maximum in May, the onshore wind stress weakens and the ARP spreads into the NBC and GC (Coles et al. 2013). This occurs synchronously with a change of the ARP from an intermediate to a fast plume structure (Geyer et al. 1996), which transports fresher water offshore. In parallel, the NBC starts to retroflect and feeds into the NECC. Both processes, the offshore transport and the retroflection, form a warm, low-salinity eddy with high productivity (Gouveia et al. 2019). During Cruise EN640, such a warm, low-salinity eddy with high productivity between 8°N and 10°N is present in Lagrangian coordinates (Fig. 3), which is consistent with the observations mentioned above. These patterns do not exist in a Eulerian coordinate system.

In the Amazon/Pará estuary, two river plumes form during peak discharge (Lentz and Limeburner 1995; Geyer et al. 1996; Smith Jr. and DeMaster 1996). These two plumes were reproduced in Lagrangian coordinates in SSS, surface nitrate concentration and turbidity, but not in a Eulerian projection (Figs. 3, 7, and 9). Subramaniam et al. (2008) showed that near shore primary production is light limited, with around 70% of total light absorption owing to CDOM. This is consistent with the near-surface PAR distribution in Lagrangian coordinates, which shows a local minimum in near-surface PAR in the inner estuary with an offshore increase that is inversely related to the decreasing turbidity. DeMaster and Pope (1996) concluded that significant nutrient uptake did not occur at salinities < 17 and suspended material concentrations > 10 mg L^{-1}. This is consistent with the local minimum in primary production rate in the estuary in Lagrangian coordinates. The influence of SSS on primary productivity is weaker near the coast and gets stronger in the offshore direction where nutrient concentration and irradiance conditions both promote phytoplankton growth (Gouveia et al. 2019). Primary productivity shows an unrealistically high rate in the inner estuary in a Eulerian system, however the productivity in Lagrangian coordinates is similar to the description of Gouveia et al. (2019) and the spatial patterns of SSS, nutrient concentration, near-surface PAR, turbidity, and productivity are dynamically consistent. These Lagrangian results are identically to the observations of Smith Jr. and DeMaster (1996) who showed that Chlorophyll concentrations were greatest in a zone located outside the turbid, high nutrient, low salinity riverine waters

but shoreward of the clear, high salinity, low nutrient waters. The observed primary productivity (Umbricht et al. 2024) is in the same range as previous observations (Smith Jr. and DeMaster 1996).

In the case of complex flow fields with high variability and low persistence, a transformation onto Lagrangian coordinates provides a synoptic picture of hydrographical measurements that is consistent with the flow fields. It is well known that advection is a nonlinear process, therefore, we strongly recommend the use of the Lagrangian method as the best way to present the distribution of biological and chemical data in systems characterized by complex and time-variant flow patterns.

One new aspect in the presented method is the use of satellite derived surface velocity fields. Although these velocity fields only reflect surface flow, the presented approach combines in situ observations with satellite data and allows deeper insight into a complex physical biological system and produces the synoptic and synchronous distributions if data interpretation is not biased.

In principle, the quality and the skill of the simulation depends on the flow field used and not on the method itself. Potential improvements could include the use of a 3-D eddy resolving circulation model, allowing 3-D advection. Further extensions could include the combination of tidal and circulation models, which would allow simulation of local tidal advection in the near-coastal area. These models are time consuming to run and require significant computational power, in contrast to our approach, which requires a run time of ~20 s per cruise on a small UNIX workstation.

Data availability statement

This study has been conducted using E.U. Copernicus Marine Service Information; DOI: 10.48670/moi-00145. The data from both Endeavor cruises are available under https://www.bco-dmo.org/project/751093. The data from the M174 Meteor cruise are available at Voss M (2021a). Master tracks in different resolutions of METEOR cruise M174, Las Palmas-Emden, 2021-2104-12–2021-2105-29. PANGAEA. doi: https://doi.pangaea.de/10.1594/PANGAEA.935041 and at Voss M et al. (2021b). Nitrogen cycling and physical processes in the Amazon River plume, Cruise No. M 174, December 4, 2021–2030/05/2021, Las Palmas (Spain)-Emden (Germany) Bonn. doi: 10.48433/cr_m174. The figures were produced with the software GrADS 2.2.1 and Golden Software Surfer 8. The transformation onto Lagrangian coordinates was calculated with a FORTRAN program developed by Ernst Maier–Reimer, which is described in details in Dippner (2005).

References

Allende-Arandia, M. E., R. Duran, L. Sanvicente-Añorva, and C. M. Apendini. 2023. Lagrangian characterization of surface transport from equatorial Atlantic to the Caribbean Sea

using climatological Lagrangian coherent structures and self-organizing maps. J. Geophys. Res. Oceans **128**: e2023JC19894. doi:10.1029/2023JC019894

Arakawa, A., and V. Lamb. 1977. Computational design of the basic dynamical processes of the UCLA general circulation model. Methods Comput. Phys. **17**: 173–265. doi:10.1016/B978-0-12-460817-7.50009-4

Arbic, B. K., R. B. Scott, D. B. Chelton, J. G. Richman, and J. F. Shriver. 2012. Effects of stencil width on surface ocean geostrophic velocity and vorticity estimation from gridded satellite altimeter data. J. Geophys. Res. Oceans **117**: 1–18. doi:10.1029/2011JC007367

Beardsley, R. C., J. Candela, R. Limeburner, W. R. Geyer, S. J. Lentz, B. M. Castro, D. Cacchione, and N. Carneiro. 1995. The M_2 tide on the Amazon shelf. J. Geophys. Res. **100**: 2283–2319. doi:10.1029/94JC01688

Berntsen, J., D. W. Skagen, and E. Svendsen. 1984. Modelling the transport of particles in the North Sea with reference to sandeel larvae. Fish. Oceanogr. **3**: 81–91. doi:10.1111/j.1365-2419.1994.tb00051.x

Bombar, D., P. H. Moisander, J. W. Dippner, R. A. Foster, M. Voss, B. Karfeld, and J. P. Zehr. 2011. Distribution of diazotrophic microorganisms and nifH gene expression in the Mekong River plume during intermonsoon. Mar. Ecol. Prog. Ser. **424**: 39–53. doi:10.3354/meps08976

Bork, I., and E. Maier-Reimer. 1978. On the spreading of power plant cooling water in a tidal river applied to the river Elbe. Adv. Water Res. **1**: 161–168. doi:10.1016/0309-1708(78)90027-1

Bourles, B., Y. Gouriou, and R. Chuchla. 1999. On the circulation in the upper layer of the western equatorial Atlantic. J. Geophys. Res. Ocean **104**: 21151–21170. doi:10.1029/1999JC900058

Brockmann, C. W., and J. W. Dippner. 1987. Tidal correction of hydrographic measurements. Dtsch. Hydrogr. Z. **40**: 241–260. doi:10.1007/BF02226279

Calef, G. W., and G. D. Grice. 1967. Influence of the Amazon River outflow on the ecology of the western tropical Atlantic II. Zooplankton abundance, copepod distribution, with remarks on the fauna of low-salinity area. J. Mar. Res. **25**: 84–94 https://elischolar.library.yale.edu/journal_of_marine_research/1087.

Choisnard, N., E. Burtscher, S. Forster, C. Frey, M. Moros, and M. Voss. 2023. The Amazon shelf sediments, a reactor that fuels intense nitrogen cycling at the seabed. Limnol. Oceanogr. **68**: 2211–2226. doi:10.1002/lno.12416

Coles, V. J., M. T. Brooks, J. Hopkins, M. R. Stukel, P. L. Yager, and R. R. Hood. 2013. The pathways and properties of the Amazon river plume in the tropical North Atlantic Ocean. J. Geophys. Res. Oceans **118**: 6894–6913. doi:10.1002/2013JC008981

Curtin, T. B. 1986a. Physical observations in the plume region of the Amazon River during peal discharge–II. Water masses. Cont. Shelf Res. **6**: 53–71. doi:10.1016/0278-4343(86)90053-1

Curtin, T. B. 1986b. Physical observations in the plume region of the Amazon River during peal discharge – III. Currents. Cont. Shelf Res. **6**: 73–86. doi:10.1016/0278-4343(86)90054-3

Curtin, T. B., and R. V. Legeckis. 1986. Physical observations in the plume region of the Amazon River during peal discharge – I. Surface variability. Cont. Shelf Res. **6**: 31–51. doi:10.1016/0278-4343(86)90052-x

Dai, A., and K. E. Trenberth. 2002. Estimates of freshwater discharge from continents: Latitudinal and seasonal variations. J. Hydrometeorol. **3**: 660–687. doi:10.1175/1525-7541(2002)003<0660:EOFDFC>2.0.CO;2

Defant, A. 1950. Reality and illusion in oceanographic surveys. J. Mar. Res. **9**: 120–138 https://elischolar.library.yale.edu/journal_of_marine_research/726

Del Vecchio, R., and A. Subramaniam. 2004. Influence of the Amazon River on the surface optical properties of the western tropical North Atlantic Ocean. J. Geophys. Res. **109**: C11001. doi:10.1029/2004JC002503

DeMaster, D. J., and R. Pope. 1996. Nutrient dynamics in Amazon shelf waters: Results from AMASSEDS. Cont. Shelf Res. **16**: 263–289. doi:10.1016/0278-4343(95)00008-O

Dippner, J. W. 1983. A hindcast of the Bravo Ekofisk blow-out. Veröffentlichung des Instituts für Meeresforschung Bremerhaven. **19**: 245–257.

Dippner, J. W. 1990. Eddy-resolving modelling with dynamically active tracers. Cont. Shelf Res. **10**: 87–101. doi:10.1016/0278-4343(90)90037-M

Dippner, J. W. 1993a. A Lagrangian model of phytoplankton growth dynamics for the northern Adriatic Sea. Cont. Shelf Res. **13**: 331–355. doi:10.1016/0278-4343(93)90113-C

Dippner, J. W. 1993b. A frontal resolving model for the German bight. Cont. Shelf Res. **13**: 49–66. doi:10.1016/0278-4343(93)90035-V

Dippner, J. W. 2005. Mathematical modelling of the transport of pollution in the water. In: Mathematical Models. *In* J. A. Filar [ed.], Encyclopedia of life support systems (EOLSS), developed under the auspices of the UNESCO. EOLSS Publishers.

Dippner, J. W., N. L. Nguyen, H. Doan-Nhu, and A. Subramaniam. 2011. A model for the prediction of harmful algae blooms in the Vietnamese upwelling area. Harmful Algae **10**: 606–611. doi:10.1016/j.hal.2011.04.012

Dippner, J. W., I. Bartl, E. Chrysagi, P. Holtermann, A. Kremp, F. Thoms, and M. Voss. 2019. Lagrangian residence time in the bay of Gdansk, Baltic Sea. Front. Mar. Sci. **6**: 725. doi:10.3389/fmars.2019.00725

Fajardo-Urbina, J. M., G. Arts, U. Gräwe, H. J. H. Clercx, T. Gerkema, and M. Duran-Matute. 2023. Atmospherically driven seasonal and interannual variability in the Lagrangian transport time scales of a multiple-inlet coastal system. J. Geophys. Res. Oceans **128**: e2022JC019522. doi:10.1029/2022JC019522

Flagg, C. N., R. L. Gordon, and S. McDowell. 1986. Hydrographic and current observations on the continental slope

and shelf of the Western equatorial Atlantic. J. Phys. Oceanogr. **16**: 1412–1429. doi:10.1175/1520-0485(1986)016<1412:HACOOT>2.0.CO;2

Fratantoni, D. M., W. E. Johns, and T. L. Townsend. 1995. Rings of the North Brazil current: Their structure and behaviour inferred frm observations and a numerical simulation. J. Geophys. Res. **100**: 10633–10654. doi:10.1029/95JC00925

Fratantoni, D. M., and D. A. Glickson. 2002. North Brazil current ring generation and evolution observed with sea WiFS. J. Phys. Oceanogr. **32**: 1058–1074. doi:10.1175/1520-0485(2002)032<1058:NBCRGA>2.0.CO;2

Geyer, W. R., and others. 1991. The physical oceanography of the Amazon outflow. Oceanography **4**: 8–14. doi:10.5670/oceanog.1991.15

Geyer, W. R., and R. C. Beardsley. 1995. Introduction to special section on physical oceanography of the Amazon shelf. J. Geophys. Res. **100**: 2281–2282. doi:10.1029/94JC03130

Geyer, W. R., R. C. Beardsley, S. J. Lentz, J. Candela, R. Limeburner, W. E. Johns, B. M. Castro, and I. D. Soares. 1996. Physical oceanography of the Amazon shelf. Cont. Shelf Res. **16**: 575–616. doi:10.1016/0278-4343(95)00051-8

Gibbs, R. J. 1970. Circulation in the Amazon River estuary and adjacent Atlantic Ocean. J. Mar. Res. **28**: 113–123 https://elischolar.library.yale.edu/journal_of_marine_research/1177

Goes, J. I., and others. 2014. Influence of the Amazon River discharge on the biogeography of phytoplankton communities in the western tropical North Atlantic. Prog. Oceanogr. **120**: 29–40. doi:10.1016/j.pocean.2013.07.010

Good, S., and others. 2020. The current configuration of the OSTIA system for operational production of Foundation Sea surface temperature and ice concentration analyses. Remote Sens. (Basel) **12**: 720. doi:10.3390/rs12040720

Gouveia, N. A., D. F. M. Gherardi, F. H. Wagner, E. T. Paes, V. J. Coles, and L. E. O. C. Aragao. 2019. The salinity structure of the Amazon River plume drives spatiotemporal variation of the oceanic primary productivity. J. Geophys. Res. Biogeo. **124**: 147–165. doi:10.1029/2018JG004665

Hart–Davis, M. G., G. Piccioni, D. Dettmering, C. Schwatke, M. Passaro, and F. Seitz. 2021. EOT20: a global ocean tide model from multi-mission satellite altimetry. Earth Syst. Sci. Data **13**: 3869–3884. doi:10.5194/essd-13-3869-2021

Johns, W. E., T. N. Lee, F. A. Schott, R. J. Zantopp, and R. H. Evans. 1990. The north brasil current retroflection: Seasonal structure and eddy variability. J. Geophys. Res. **95**: 22103–22120. doi:10.1029/JC095iC12p22103

Kalnay, E., and others. 1996. The NCEP/NCAR reanalysis 40-year project. Bull. Am. Met. Soc. **77**: 437–471. doi:10.1175/1520-0477(1996)077<0437:TNYRP>2.0.CO;2

Körtzinger, A. 2003. A significant CO_2 sink in the tropical Atlantic Ocean associated with the Amazon River plume. Geophys. Res. Lett. **30**: 1–4. doi:10.1029/2003GL018841

Kuhn, A. M., M. Mazloff, S. Dutkiewicz, O. Jahn, S. Clayton, T. Rynearson, and A. D. Barton. 2023. A global comparison of marine chlorophyll variability observed in Eulerian and Lagrangian perspectives. J. Geophys. Res. Oceans **128**: e2023JC019801. doi:10.1029/2023JC019801

Lagerloef, G. S. E., G. T. Mitchum, R. B. Lukas, and P. P. Niiler. 1999. Tropical Pacific near-surface currents estimated from altimeter, wind, and drifter data. J. Geophys. Res. **104**: 23313–23326. doi:10.1029/1999JC900197

Lentz, S. J. 1995a. The Amazon River plume during AMASSEDS: Subtidal current variability and the importance of wind forcing. J. Geophys. Res. **100**: 2377–2390. doi:10.1029/94JC00343

Lentz, S. J. 1995b. Seasonal variations in the horizontal structure of the Amazon plume inferred from historical hydrographic data. J. Geophys. Res. **100**: 2391–2400. doi:10.1029/94JC01847

Lentz, S. J., and R. Limeburner. 1995. The Amazon River plume during AMASSEDS: Spatial characteristics and salinity variability. J. Geophys. Res. **100**: 2355–2375. doi:10.1029/94JC01411

Limeburner, R., R. C. Beardsley, I. D. Soares, S. J. Lentz, and J. Candela. 1995. Lagrangian flow observations of the Amazon River discharge into the North Atlantic. J. Geophys. Res. **100**: 2401–2415. doi:10.1029/94JC03223

Liu, W., and N. Sneeuw. 2021. Aliasing of ocean tides in satellite gravimetry: A two-step mechanism. J. Geod. **95**: 134. doi:10.1007/s00190-021-01586-5

Loick-Wilde, N., S. C. Weber, B. J. Conroy, D. G. Capone, V. J. Coles, P. M. Medeiros, D. K. Steinberg, and J. P. Montoya. 2016. Nitrogen sources and net growth efficiency of zooplankton in three Amazon River plume food webs. Limnol. Oceanogr. **61**: 460–481. doi:10.1002/lno.10227

Maier–Reimer, E. 1977. Residual circulation in the North Sea due to M_2–tide and mean annual wind stress. Dtsch. Hydrogr. Z. **30**: 69–80. doi:10.1007//BF02227045

Maier–Reimer, E. 1978. On the formation of salt wedges in estuaries, p. 91–101. *In* J. Sündermann and K. P. Holz [eds.], Mathematical modelling in estuarine physics. Springer Verlag.

Maier–Reimer, E. 1979. Some effects of Atlantic circulation and of river discharges on the residual circulation of the North Sea. Dtsch. Hydrogr. Z. **32**: 126–130. doi:10.1007/BF02227000

Maier–Reimer, E. 1988. Vorticity balance in gulfstream trajectories. Ocean Model. **76**: 9–11.

Meade, R. H., T. Dunne, J. E. Ritchey, U. M. Santos, and E. Salati. 1985. Storage and remobilization of suspended sediment in the lower Amazon River of Brazil. Science **228**: 488–490. doi:10.1126/science.228.4698.488

Molinari, R. L. 1983. Observations of near-surface currents and temperature in the central and Western tropical Atlantic Ocean. J. Geophys. Res. **88**: 4433–4438. doi:10.1029/JC088iC07p04433

Montoya, J. P., J. P. Landrum, and S. C. Weber. 2019. Amazon River influence on nitrogen fixation in the western tropical North Atlantic. The sea: The current and future ocean. J. Mar. Res. **77**: 191–213. doi:10.1357/002224019828474278

Müller-Karger, F. E., C. R. McClain, and P. L. Richardson. 1988. The dispersal of Amazon's water. Nature **333**: 56–59. doi:10.1038/333056A0

NASA. 1989. Ocean color from space. Woods Hole Mass., InterNetwork Inc, p. 7.

Neto, A.v. N., and A. S. Silva. 2014. Seawater temperature changes associated the the North Brazil current dynamics. Ocean Dyn. **64**: 13–27. doi:10.1007/s10236-013-0667-4

Nittrouer, C. A., and others. 1991. Sedimentology and stratigraphy of the Amazon continental shelf. Oceanography **4**: 33–38. doi:10.5670/oceanog.1991.19

Oltman, R. E. 1968. Reconnaissance investigations of the discharge and water quality of the Amazon River. US Geol. Surv. Circ. **552**: 16.

Pavia, E. G., and B. Cushman–Roisin. 1988. Modelling oceanic fronts using particle method. J. Geophys. Res. **93**: 3554–3562. doi:10.1029/JC093iC04p03554

Pham, A. H., N. Choisnard, A. Fernandez-Carrera, A. Subramaniam, E. K. Strope, E. J. Carpenter, M. Voss, and J. P. Montoya. 2024. Planktonic habitats in the Amazon plume region of the Western tropical North Atlantic. Front. Mar. Sci. **11**: 1287497. doi:10.3389/fmars.2024.1287497

Pujol, M. I., Y. Faugere, G. Taburete, S. Dupuy, C. Pelloquin, M. Ablain, and N. Picot. 2016. DUACS ST2014: The new multi-mission altimeter data set reprocessed over 20 years. Ocean Sci. **12**: 1067–1090. doi:10.5194/os-12-1067-2016

QUID. 2018. Quality information document for sea level TAC DUACS products EU copernicus marine environment monitoring service, v. **66**. QUID. http://Marine.Copernicus.Eu/Documents/QUID/CMEMS-SL-QUID-008-032-051.pdf

Richardson, P. L., and G. Reverdin. 1987. Seasonal cycle of velocity in the Atlantic north equatorial countercurrent as measured by surface drifters, current meters and ship drifts. J. Geophys. Res. **92**: 3691–3708. doi:10.10029/JC092iC04p03691

Roache, P. J. 1976. Computational fluid dynamics. Hermosa Publisher, p. 446.

Ryther, J. H., D. W. Menzel, and N. Corwin. 1967. Influence of the Amazon River outflow on the ecology of the western tropical Atlantic. I. Hydrography and nutrient chemistry. J. Mar. Res. **25**: 69–83 https://elischolar.library.yale.edu/journal_of_marine_research/1086.

Sathyendranath, S., and others. 2019. An ocean-colour time series for use in climate studies: The experience of the ocean-colour climate change initiative (OC-CCI). Sensors **19**: 4285. doi:10.3390/s19194285

Smith, W. O., Jr., and D. J. DeMaster. 1996. Phytoplankton biomass and productivity in the Amazon River plume: Correlation with seasonal river discharge. Cont. Shelf Res. **16**: 291–319. doi:10.1016/0278-4343(95)00007-N

Stramma, L., and F. Schott. 1999. The mean flow field in the tropical Atlantic Ocean. Deep Sea Res. II **46**: 279–303. doi:10.1016/S0967-0645(98)00109-X

Subramaniam, A., and others. 2008. Amazon River enhances diazotrophy and carbon sequestration in the tropical North Atlantic Ocean. Proc. Natl. Acad. Sci. U. S. A. **105**: 10460–10465. doi:10.1073/pnas.0710279105.0710279105

Tomczak, M., and J. S. Godfrey. 1994. Regional oceanography: An introduction. Pergamon Press, p. 442.

Tyaquiçã, P., D. Veleda, N. Lefevre, M. Araujo, C. Noriega, G. Caniaux, J. Servain, and T. Silva. 2017. Amazon plume salinity response to ocean teleconnections. Front. Mar. Sci. Sec. Aquat. Microbiol. **4**: 2017. doi:10.3389/fmars.2017.00250

Umbricht, J., C. Burmeister, J. W. Dippner, I. Liskow, J. P. Montoya, A. Subramaniam, and M. Voss. 2024. Nitrate uptake and primary production along the Amazon River plume continuum. J. Geophys. Res. Biogeosci. submitted.

Voss M. 2021a. Master tracks in different resolutions of METEOR cruise M174, Las Palmas-Emden, 2021-2104-12–2021-2105-29. PANGAEA. doi: https://doi.pangaea.de/10.1594/PANGAEA.935041

Voss M. 2021b. Nitrogen cycling and physical processes in the Amazon River plume, Cruise No. M 174, December 4, 2021–2030/05/2021, Las Palmas (Spain)-Emden (Germany) Bonn. doi:10.48433/cr_M174

Weber, S. C., E. J. Carpenter, V. J. Coles, P. L. Yager, J. Goes, and J. P. Montoya. 2017. Amazon River influence on nitrogen fixation and export production in the western tropical North Atlantic. Limnol. Oceanogr. **62**: 618–631. doi:10.1002/lno.10448

Weber, S. C., A. Subramaniam, J. P. Montoya, H. Doan-Nhu, L. Nguyen-Ngoc, J. W. Dippner, and M. Voss. 2019. Habitat delineation in highly variable marine environments. Front. Mar. Sci. **6**: 112. doi:10.3389/fmars.2019.00112

Woods, J. D., and R. Onken. 1982. Diurnal variation and primary production in the ocean -preliminary results of a Lagrangian ensemble model. J. Plankton Res. **4**: 735–756. doi:10.1093/plankt/4.3.735